

1                   **Implications on large-scale flow of the fractured**  
2                   **EGS reservoir Soultz inferred from hydraulic**  
3                   **data and tracer experiments**

4  
5   Name of authors:

6   Egert, Robert<sup>a</sup>; Gholami Korzani, Maziar<sup>a</sup>; Held, Sebastian<sup>a</sup>; Kohl, Thomas<sup>a</sup>

7   E-Mail addresses:

8   robert.egert@kit.edu, m.gholami@kit.edu, sebastian.held@kit.edu, thomas.kohl@kit.edu

9   Addresses:

10   <sup>a</sup>Institute of Applied Geosciences, Karlsruhe Institute of Technology, Adenauerring 20b, 76131

11   Karlsruhe, Germany

12

13 **Implications on large-scale flow of the fractured**  
14 **EGS reservoir Soultz inferred from hydraulic data**  
15 **and tracer experiments**

16 Egert, Robert; Gholami Korzani, Maziar; Held, Sebastian; Kohl, Thomas

17 **Abstract**

18 The Enhanced geothermal system in Soultz-sous-Forêts, located in the geothermal favorable Upper  
19 Rhine Graben, is a fracture-controlled reservoir that was highly investigated in the last decades  
20 generating a huge geoscientific database. Numerical reservoir models use this database to simulate  
21 the operation of the subsurface heat exchanger, yet suffer from simplifications regarding the transfer  
22 of experimental into model data, dimensional extension, and computational power and efficiency.  
23 The new extensive transient 3-D simulations, based on geophysical, geological and hydraulic data,  
24 highlight the hydraulic and transport feedback of the Soultz EGS due to convective and advective  
25 fluid flow. Developed with the goal of simulating the vast tracer test data during the reservoir-testing  
26 phase in 2005, the Finite Element Model is focusing on the main fractured zones, which connect the  
27 wells in the deep reservoir. It comprises 13 major hydraulically active faults and fractures in a  
28 13x11x5 km extending model domain, as well as open-hole sections of the wells GPK1 to GPK4 and  
29 their casing leakages. The simulation of the tracer experiment confirms the strong heterogeneity of  
30 the reservoir and highlights the importance of a potential fractured zone, hydraulically separating the  
31 reservoir in a northern (GPK1 to 3) and southern section (GPK4). This zone tends to connect the  
32 reservoir to the main fault system by hydraulically separating GPK4 from the other wells. The  
33 calibration and sensitivity analyses provide a unique, broad understanding of the reservoir flow zones  
34 providing information on the extension of the Soultz reservoir in the future and on the fluid pathways  
35 in the deep subsurface of the Upper Rhine Graben.

36 **Keywords**

37 Enhanced Geothermal System; Soultz-sous-Forêts; Discrete Fracture Network; tracer experiment;  
38 Finite Element, transport modeling

39 **1. Introduction**

40 The Upper Rhine Graben (URG) is one of the most distinct areas in central Europe for the utilization  
41 of geothermal energy. Favorable thermal conditions with gradients of greater than 100 K.km<sup>-1</sup>  
42 (Pribnow and Schellschmidt, 2000) have led to the development of several successful power plant  
43 projects targeting the hydrothermal sedimentary cover and the deep crystalline basement of the  
44 URG as Enhanced Geothermal System (EGS) (Genter et al., 2016; Vidal and Genter, 2018). EGS  
45 are designed to take advantage of natural permeable faults and fractures and improve their natural

46 hydraulic properties through chemical and hydraulic stimulation (Schindler et al., 2010). One of the  
47 first and most prominent European EGS is located at Soultz-sous-Forêts (Garnish, 2002; Gérard et  
48 al., 2006), targeting a fractured geothermal reservoir in a depth of up to 5000 m and temperatures  
49 up to 200 °C (Genter et al. 2010). Starting in the 1980s, a unique scientific database has been  
50 created, which opens the opportunity to study hydraulic processes in the geothermal reservoir, and  
51 especially along faults and fractures and on the matrix-fracture-interface (Genter et al., 2010; Sausse  
52 et al., 2010).

53 Various experiments, such as tracer and circulations tests, were conducted to characterize and  
54 quantify fluid flow through a single fracture or fracture networks not only in the Soultz EGS but in  
55 laboratory and field experiments worldwide (Berkowitz, 2002). In laboratory scale, single fracture  
56 geometries were often described as self-affine rough surfaces with varying apertures exposed to  
57 laminar and/or turbulent fluid flow (Schmittbuhl et al., 2008). Meter-scale migration experiments,  
58 conducted in Underground Research Laboratories, considered fractures as shear zones with a high  
59 number of small discrete channels (Hadermann and Heer, 1996). Typically, Darcy flow was assumed  
60 within the shear zone (Moreno et al., 1988). In the reservoir scale, the geometry, interconnection,  
61 and behavior of fractures are sparsely known and accessible since wellbores and experiments  
62 provide point-like information of shape and fracture density (Dezayes et al., 2010) while geophysical  
63 measurements show the spatial distribution (Sausse et al., 2010). Detailed information about the  
64 reservoir hydraulics, including the reservoir fluid migration pathways, mean residence times, swept  
65 pore volume and heat exchange area between different wells, can be achieved using inter-well tracer  
66 experiments (Robinson and Tester, 1984). In the past, several tracer experiments were conducted  
67 in enhanced geothermal reservoirs which, however, were assumed to be simplified connections  
68 between two wells as a single planar structure or ideal fracture network when attempting to model  
69 (Ayling et al., 2016; Ghergut et al., 2016; Iglesias et al., 2015; Karmakar et al., 2016; Rose et al.,  
70 2009; Sanjuan et al., 2006).

71 An elegant way to resolve arisen issues of missing spatial information and unconnected data is to  
72 simultaneously apply structural and numerical models for investigating the natural and forced hydro-  
73 thermal processes of an EGS (O'Sullivan et al., 2001). Various numerical studies of the Soultz  
74 geothermal reservoir have been conducted over decades for investigating different physical  
75 processes, such as natural convection (Bächler et al., 2003; Guillou-Frottier et al., 2013; Kohl et al.,  
76 2000; Vallier et al., 2019) and the effects of mechanical stimulation to the reservoir performance  
77 (Baujard and Bruel, 2006; Kohl et al., 2006; Kohl and Mégel, 2007). Furthermore, inter-well  
78 circulation was investigated by fitting analytical and numerical solutions to the measured tracer data.  
79 Sanjuan et al. (2006) applied an analytical dispersive transfer model while Blumenthal et al. (2007)  
80 and Gessner et al. (2009) presented simplified models for the direct circulation between GPK3 and  
81 GPK2 wells. Kosack et al. (2011) compared three different inversion methods to evaluate their

82 applicability to the connection between GPK3 and GPK2. Vogt et al. (2012) applied the Ensemble  
83 Kalman Filter (EnKF) to individually invert for the concentrations measured at GPK2 and GPK4.  
84 Gentier et al. (2010; 2011) developed a first Discrete Fracture Network (DFN) considering  
85 hydraulically active parts and fracture sets and independently adapted the model for both wells using  
86 a particle tracking method. It was concluded that it is not possible to create a single homogeneous  
87 statistical fracture model that reproduces both wells simultaneously, as the main structure interferes  
88 with the hydraulic field between GPK3 and GPK4. Radilla et al. (2012) fitted a model to the  
89 experimental data, connecting the individual wells on three independent and isolated pathways with  
90 an equivalent stratified medium approach. All authors commonly conclude that a single-fracture  
91 approach is not suitable to sufficiently describe the hydraulic flow in the complex Soultz geothermal  
92 reservoir.

93 EGS are often simplified as theoretical/hypothetical fracture systems, connecting two wells along a  
94 line or one or more parallel plates (Bataillé et al., 2006; Fox et al., 2013; Vallier et al., 2019). It is  
95 known from the well-developed Soultz geothermal reservoir that this assumption does not  
96 adequately describe the structure of the heat exchanger system in an EGS (Genter et al., 2010).  
97 The understanding of the complex faults & fractures pattern and thus, on the tectonic history,  
98 preferential flow paths and hydrothermal circulations are crucial for the sustainable and safe design  
99 of a geothermal operation avoiding any artificially induced risks, like thermal breakthrough or induced  
100 seismicity (Zang et al., 2014). Therefore, the goal of the present study is a qualitative and quantitative  
101 evaluation of naturally and artificially induced fluid flow in a complex fractured geothermal reservoir  
102 to further investigate impacts of the considered limiting assumptions in the literature and better  
103 understand complex fluid circulation. Moreover, the knowledge gained allows the optimization of the  
104 design of future experiments and operation scenarios and the prediction of expected results (Kohl  
105 and Mégel, 2007).

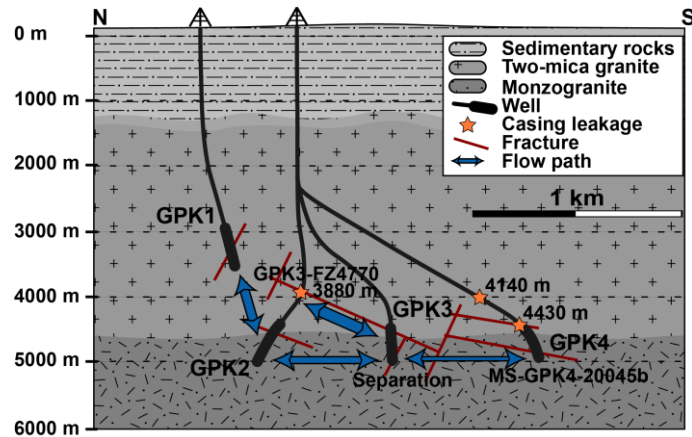
106 Herein, we present an extensive numerical study including the large structural complexity of the  
107 Soultz fault and fracture network solving a transient fully-coupled Hydro-Solute (HS) transport  
108 simulation with the TIGER code. The three-dimensional flow field and tracer propagation in the  
109 Soultz geothermal reservoir are predicted and represent a major extension of an earlier approach  
110 by Held et al. (2014). The model includes the granitic basement as well as several hydraulically  
111 active faults and fractures as discrete surfaces and the open-hole sections of the wells as discrete  
112 line features. Long-term inter-well circulation tests are initially used to forward invert the hydraulic  
113 parameters of the fracture network while the hydraulic model is further recalibrated to reproduce the  
114 inter-wells tracer experiment (Sanjuan et al., 2006). The combination of the numerical approach with  
115 different kind of experimental data allows quantification and evaluation of the flow field inside the  
116 heat exchanger of the Soultz EGS and the identification of inter-well connections over the complex

117 fracture network. The numerical approach allows a detailed characterization of the subsurface heat  
118 exchanger with the possibility to recognize feasible features for future expansion.

## 119 **2. The Soultz geothermal reservoir**

120 The Soultz geothermal system is located in the French-side of the central URG, which is part of the  
121 “European Cenozoic Rift System” extending from southern France to the North Sea (Ziegler and  
122 Dèzes, 2005). The major tectonic feature of the Soultz reservoir is a horst structure uplifting the  
123 Soultz reservoir between Hermerswiller and Kutzenhausen fault, narrowing the Cenozoic and  
124 Mesozoic cover to a thickness of 1400 m (Aichholzer et al., 2016). The underlying crystalline  
125 basement is characterized as a low-permeable naturally fractured rock (Hooijkaas et al., 2006;  
126 Sausse and Genter, 2005) with an alteration-dependent rock matrix permeability ranging from  $10^{-19}$   
127  $\text{m}^2$  to  $10^{-20}$   $\text{m}^2$  (Hettkamp et al., 1999). The existing fault- and fracture-system is a result of the  
128 tectonic history of the URG. The dominant fracture orientation ( $160 \pm 15^\circ$ ) is linked to the recent  
129 maximum horizontal stress orientation of  $170 \pm 10^\circ$  (Cornet et al., 2007; Evans et al., 1997). Other  
130 fracture sets are oriented with Rhenish ( $20 \pm 10^\circ$ ) and Hercynian ( $130 \pm 10^\circ$ ) orientation with a steep  
131 dip ( $>60^\circ$ ) to the west (Dezayes et al., 2010). The mean aperture is varying between 0.1 mm and  
132 250 mm (Dezayes et al., 2010). Fractures oriented parallel to the main stress field tend to remain  
133 open and thus contain increased permeability (Cornet et al., 2007), while those perpendicular or  
134 orthogonal to the main stress field have the tendency to be sealed.

135 As shown in Fig. 1, the Soultz EGS can be divided into three sub-reservoirs (2000 m, 3500 m, and  
136 5000 m) and utilized by four wells (GPK1 to GPK4) (Schill et al., 2017). The boreholes were drilled  
137 into the western flank of the Soultz horst structure. The GPK1 well targets the middle reservoir with  
138 a maximum depth of 3600 m while GPK2 to GPK4 were drilled over 5000 m depth to exploit the  
139 deeper crystalline reservoir (Genter et al., 2010). The lowest 500 - 700 m section of each borehole  
140 is not equipped with a casing and left completely open against the rock. The remaining part is cased  
141 with leakages reported for GPK2 and GPK4 (Pfender et al., 2006). The leakage of the well GPK2 at  
142 the depth of 3880 m connects GPK2 to the major fractured and altered zone GPK3-FZ4770 and  
143 thereon to the well GPK3 (Sausse et al., 2010). Jung et al. (2010) concluded a fluid loss of more  
144 than 16 % in the leakage of GPK2 measured with the brine displacement method. The three deep  
145 wells are aligned NNW-SSE with a lateral distance of 650 m in a depth of 5000 m while the distance  
146 between GPK1 and GPK2 is 450 m.



147

148 *Fig. 1: 2D-Subset of the geological setting of the Soutz geothermal reservoir including wells, open-hole sections, and the*  
 149 *considered lithological units. The main fractures are shown as red lines; the expected hydraulic connections based on*  
 150 *Sanjuan et al. (2006) and Aquilina et al. (2004) are shown in blue; orange stars indicate the reported casing leakages*

151 Circulation and inter-well tracer experiments allow the prediction of forced fluid flow and the hydraulic  
 152 quantification of the connection between the individual wells, while spatial information, e.g. on the  
 153 flow paths within the reservoir, is not known (Ghergut et al., 2013). At the Soutz site, several  
 154 experiments have been conducted with different well setups during the long-term research activities  
 155 (Schill et al., 2017). A tracer experiment carried out in 1997 examined the connection of GPK1 and  
 156 GPK2 (Aquilina et al., 1998), while a tracer experiment in 2005 further focused on the main hydraulic  
 157 connections in the deeper reservoir between GPK2, GPK3, and GPK4. Sanjuan et al. (2006)  
 158 concluded two connections between GPK3 and GPK2 through a hydraulic short-circuit and an  
 159 additional pathway of elevated length, while a poor link between GPK3 and GPK4 was observed.  
 160 Further inter-well tracer experiments have been conducted confirming the main findings of this  
 161 experiment (Sanjuan et al., 2015).

### 162 3. Numerical modeling

163 The numerical simulations are carried out with a Finite-Element (FE) open-source application called  
 164 TIGER (THC simulator for GEoscience Research) (Gholami Korzani et al., 2019), which is based on  
 165 MOOSE (Multiphysics Object-Oriented Simulation Environment) framework (Gaston et al., 2009).  
 166 TIGER has been developed to tackle thermo-hydraulic-solute transport problems in geothermal  
 167 reservoirs including lower-dimensional features for fractures and well paths.

#### 168 3.1. Governing equations

169 The approach assumes a Representative Elementary Volume (REV) for the porous media where  
 170 interaction between the coupled processes can occur (Bear and Cheng, 2010). The hydraulic field  
 171 is solved for the pore pressure by combining mass and momentum balances including Darcy's law  
 172 (Bundschuh et al., 2010) as:

$$bS_m \frac{\partial P}{\partial t} + \nabla \cdot b\mathbf{q} = Q \quad \text{Eq. 1}$$

$$\mathbf{q} = \frac{\mathbf{k}}{\mu} (-\nabla P + \rho^l \mathbf{g}) \quad \text{Eq. 2}$$

173 where  $P$  is the pore pressure;  $t$  is the time;  $S_m$  is the mixture specific storage of the liquid and solid  
 174 phase;  $Q$  is the source term for injection and production;  $\mathbf{k}$  is the permeability tensor;  $\mu$  is the fluid  
 175 dynamic viscosity;  $\rho^l$  is the fluid density;  $\mathbf{g}$  is the gravitational acceleration vector;  $\mathbf{q}$  is the fluid or  
 176 Darcy velocity vector and  $b$  is the scale factor for considering fractures (aperture) and wells (area).  
 177 Lower-dimensional fractures are treated as discrete 2D elements while open-hole sections are  
 178 discretized as 1D elements, sharing nodes, faces, and lines with the 3D continuum.

179 The transport of solutes (e.g. tracers) is considered as spatial and temporal changes of concentration  
 180 which are governed by an advection-diffusion-dispersion equation (Bear and Cheng, 2010).

$$b \frac{\varphi \partial C}{\partial t} + b(-\nabla \cdot \mathbf{D}_m \nabla C + \mathbf{q} \nabla \cdot C) = Q \quad \text{Eq. 3}$$

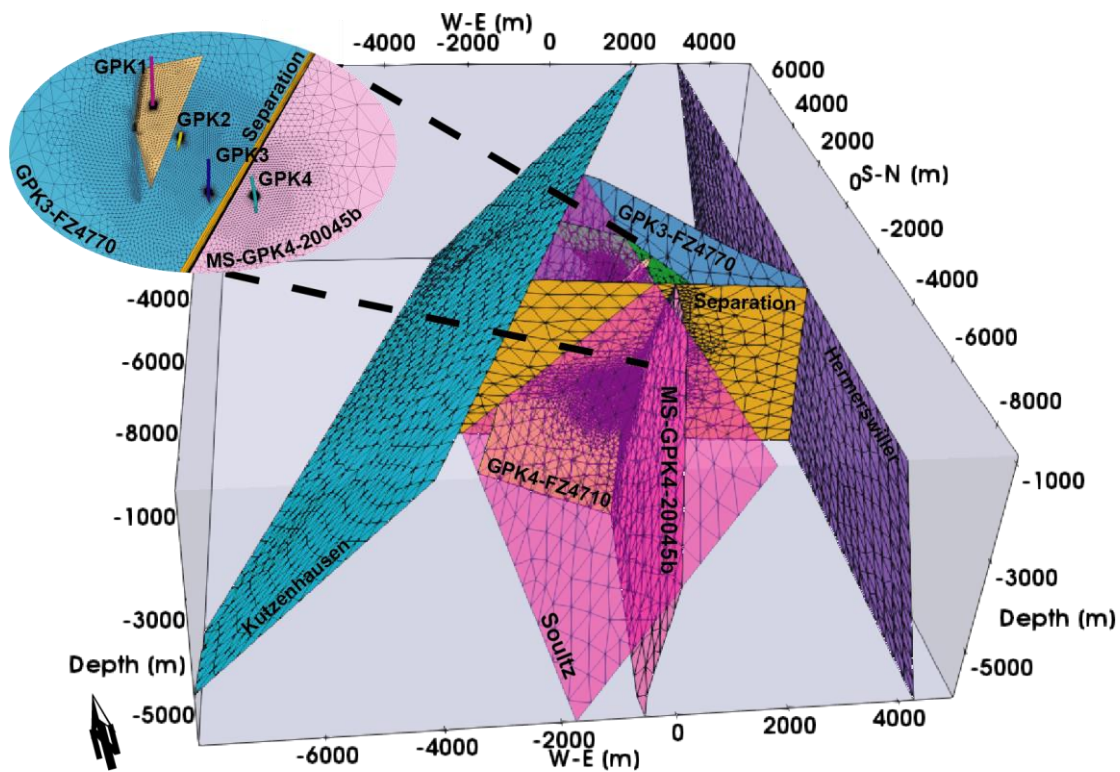
181 where  $C$  is the solute concentration;  $\varphi$  is the porosity;  $\mathbf{D}_m$  is the sum of molecular diffusion and  
 182 dispersion. The dispersion tensor is dependent on Darcy velocity and longitudinal and transversal  
 183 dispersivity (Bear and Cheng, 2010), which generally describes the mixing around maximum  
 184 concentration due to different mechanical effects (Bauget and Fourar, 2007).

### 185 3.2. Numerical model

186 A 3D-Discrete Fracture Matrix (DFM) model is used to ensure high accuracy in the geometrically  
 187 complex reservoir by considering DFN and the surrounding matrix in the numerical analysis (Berre  
 188 et al., 2018). The available information about the geological and tectonic settings, including well  
 189 paths and open-hole sections, can be merged into a structural model of the Soultz geothermal  
 190 reservoir. The used reservoir model, which is a subset of the structural model proposed by Sausse  
 191 et al. (2010) and Place et al. (2011), is based on the 3D-model created by Held et al. (2014).  
 192 However, the model is updated and extended in this study by introducing two additional fracture  
 193 zones as 1) the WNW-ESE-oriented fracture "Separation" between the wells GPK3 and GPK4, and  
 194 2) GPK1-FZ2856 fracture intersecting GPK1 in the middle reservoir. The Separation fracture was  
 195 not drilled but suspected as an anomalous zone of either higher permeability or hydraulic barrier,  
 196 separating the deeper reservoir into a northern and a southern part (Calò et al., 2016; Kohl et al.,  
 197 2006; Sausse et al., 2010). The fracture GPK1-FZ2856, identified using Vertical Seismic Profiling  
 198 (Sausse et al., 2010), is added to allow better adjustment of hydraulic parameters close to the GPK1  
 199 well. The model has an extension of 13 (E-W) x 11 (N-S) km with a vertical depth of 5 km (Fig. 2),  
 200 located between 1000 m and 6000 m below surface. The extension of the domain is chosen, to avoid  
 201 boundary effects on the area of interest and to possibly consider the effects of the regional flow field.  
 202 The minimum lateral distance between well and boundary is 4000 m.

203 Minor simplifications were made regarding the location, dipping and hydraulic appearance of the  
 204 fracture network by representing fractures as discrete features. Out-of-plane mixing effects like

205 surface roughness, fault gauge or internal mixing cannot be treated individually and are therefore  
 206 summarized in the hydrodynamic dispersion (Bauget and Fourar, 2007). Tsang et al. (1988)  
 207 concluded that it is suitable to use a statistically homogenous system (e.g. for aperture, permeability)  
 208 if the transport dimensions are significantly larger than the spacing between the channels belonging  
 209 to a fracture and the transport distance is large enough to remain unaffected by local heterogeneities.  
 210 The wells GPK1 to GPK4 are discretized over the entire open-hole section (and casing leakage) and  
 211 connected with at least two fractures to the reservoir. The element size differs between 1.5 m  
 212 (around and along the wells) and 500 m (close to the boundaries) with a typical element size around  
 213 40 m. As the fracture GPK3-FZ4770, establishing the main connection of GPK3 and GPK2 is inclined  
 214 and not oriented parallel to the wells, the wells intersect the fracture in different reservoir levels  
 215 resulting in the true distance of 840 m (compared to the often used 650 m derived from a pure  
 216 horizontal distance). To consider the effects of hydraulic or chemical stimulation (Nami et al. 2008;  
 217 Schill et al. 2017) and to minimize mesh dependency of the results, the main fracture GPK3-FZ4770  
 218 is subdivided and refined around GPK2 and GPK3. In total, the model contains 141'271 nodes which  
 219 are connected by 714'453 elements including 3D matrix, 13 fractures, and 4 wells as shown in Fig.  
 220 2.



221  
 222 *Fig. 2: 13-fracture-model of the Soultz geothermal reservoir including wells (modified after Held et al. (2014)). Grey shows*  
 223 *the extension of the matrix. 10 out of 13 discrete faults and fractures are shown. The central area of the mesh along GPK3-*  
 224 *FZ4770 and between GPK2, GPK3, and GPK4 is shown in detail.*

225 The pore pressure in the whole reservoir is assumed to be hydrostatic (Stober and Bucher, 2007)  
 226 by setting the top and bottom boundary conditions (BC) as Dirichlet BC and the model initial condition  
 227 (IC) in accordance. Injection and extraction rates are applied as time-dependent mass-flux-function



228 on top of each open-hole section. The matrix permeability is assumed to be orthotropic with higher  
 229 permeability in N-S-direction to take the regional stress field of the URG and small-scale fractures  
 230 into account (Cornet et al., 2007). A natural S-N-oriented graben-parallel background flux of  $1 \text{ m}^3 \cdot \text{h}^{-1}$   
 231 <sup>1</sup> (Bächler et al., 2003; Sanjuan et al., 2006) is applied to the main faults and fractures as a function  
 232 of the individual aperture.

233 The injected fluorescein tracer is assumed to be conservative in terms of reaction and sorption during  
 234 transport as well as radioactive and thermal decays (Adams and Davis, 1991; Berkowitz, 2002).  
 235 Solute diffusion, dispersion, and advection into the granitic basement are neglected (Bodin et al.,  
 236 2003), as the porosity of the matrix is significantly smaller than the ones of the DFN (Aquilina et al.,  
 237 2004). The solute (re-)injection is applied as time-dependent Dirichlet BC inferred from concentration  
 238 measurements at GPK3 wellhead. The parametrization of the matrix and fluid properties took into  
 239 account the conditions in the reservoir (e.g. increased temperature and salinity, Table 1). For  
 240 enhancing the accuracy, minimizing unwanted numerical diffusion and conservation of the sharp  
 241 concentration front, a second-order semi-implicit time-integration method (Crank and Nicolson,  
 242 1996) and a Streamline Upwind method (Brooks and Hughes, 1982) are applied.

243 *Table 1: Constant model input parameters for the fluid and solid phases, the reservoir brine properties are in accordance*  
 244 *with Kestin et al. (1981) representing a brine with 150 °C, 35 MPa and 1.5 mol.kg<sup>-1</sup> salinity*

Parameter	Value
Fluid density [kg.m <sup>-3</sup> ]	1065
Fluid dyn. viscosity [Pa.s]	$2.3 \times 10^{-4}$
Fluid compressibility [Pa <sup>-1</sup> ]	$2 \times 10^{-9}$
Matrix compressibility [Pa <sup>-1</sup> ]	$5 \times 10^{-13}$
Fracture porosity [-]	1
Matrix porosity [-]	$1 \times 10^{-2}$
Solute diffusion [m <sup>2</sup> .s <sup>-1</sup> ]	$4 \times 10^{-10}$

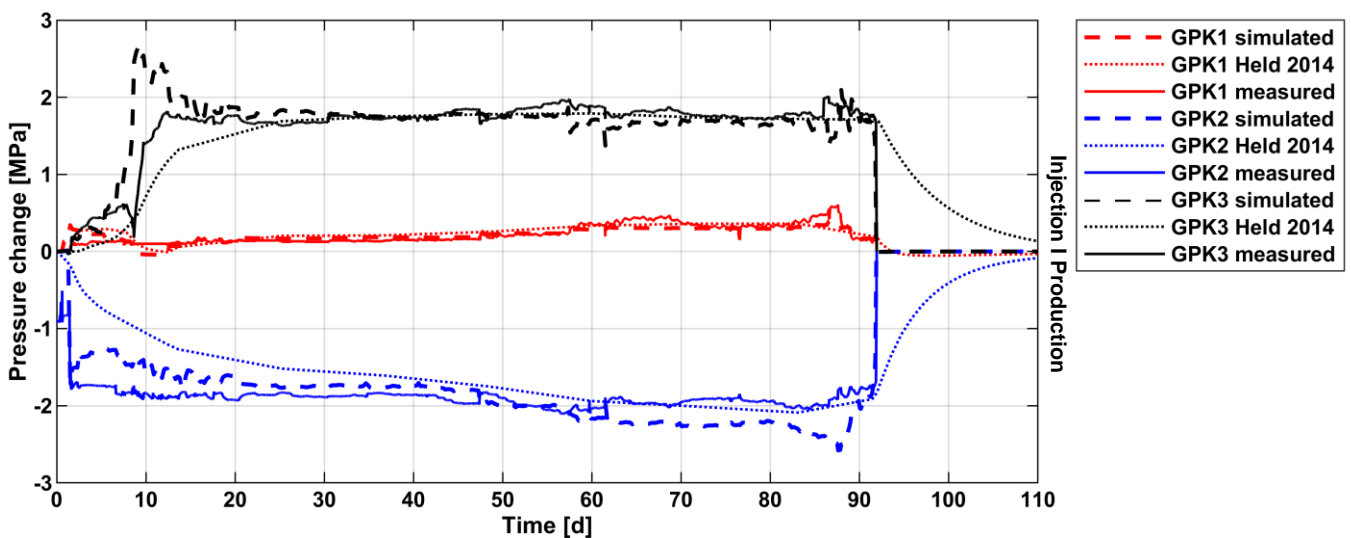
## 245 4. Results

### 246 4.1. Calibration of the hydraulic and solute processes

247 The transmissivities of the Soultz fracture network are calibrated against two circulation tests  
 248 conducted in 2009 (Schindler, 2009) and 2011 (Genter et al., 2011). Flow rate changes at wellheads  
 249 and their effects on the reservoir pore pressure were used to quantify the transmissivities of the  
 250 faults and fractures. Flow velocity logs from each borehole were used to assign the measured portion  
 251 of flux to the individual fractures since the matrix tends to have significantly lower permeability. The  
 252 calibration is necessary because two further fractures, compared to Held et al. (2014), affect the  
 253 pressure field and the capability of TIGER in applying time-dependent BCs enabling more accurate  
 254 modeling of the reservoir.

255 A circulation test, with average flowrates between 9 and 20 l.s<sup>-1</sup>, conducted in early 2011 (Genter et  
 256 al., 2011) allowed the calibration of the fractures connected to three wells of GPK1, GPK2, and GPK3  
 257 through production in GPK2 and reinjection in GPK1 and GPK3. Fig. 3 shows the pore pressure  
 258 changes at GPK1 to GPK3 after the calibration of the fractures' transmissivity. For GPK1, no flow  
 259 rate data was recorded from 8<sup>th</sup> to 10<sup>th</sup> day of the experiment leading to no flow in the simulation.  
 260 However, the pressure response almost fitted the measured data. The lower pressure increase in  
 261 GPK1, compared to GPK3, indicates a good connection of the borehole to high permeable zones.  
 262 For GPK2, the simulated data slightly underestimates the pressure response in the first 50 days,  
 263 while it overestimates later. A casing leakage was reported after day 47 (Genter et al., 2011),  
 264 affecting the experimental results. This leakage caused the fluid already pumped in the pipe to flow  
 265 back into the reservoir and led to lower measured pressure change for the measured flow rates. That  
 266 leakage was not incorporated in this study as it only affects the internal system of GPK2 well.

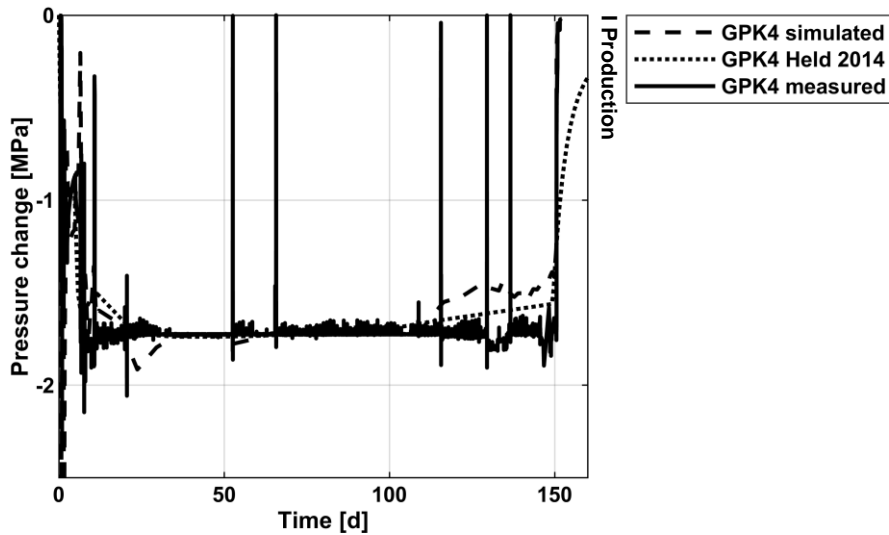
267 The measurements of GPK3 show high scattering up to 20 days, which was caused by strongly  
 268 varying flow rates at the start of the experiment. After 20 days, the flow rate was kept constant,  
 269 leading to a steady pressure change until the end of the experiment. The obtained pressure changes  
 270 for GPK3 did not well match the measured data between day 5 and 15. The missing match could be  
 271 the result of several factors like borehole or skin effects, (re-) opening of small-scale fractures,  
 272 changes in the flow regime and leakages in the tubing. Since the proposed model focusses on long-  
 273 term evaluation, the calibration was done by fitting the mean steady section of the experimental data.  
 274 It is worthwhile noting that the injection wells (GPK1 and GPK3) have almost the same average flow  
 275 rates (approx. 9 l.s<sup>-1</sup>) and at the same time have significantly different pressure responses. The  
 276 immediate pressure decline after the pump shutdown shows a small storage effect along the different  
 277 fractures and the granitic matrix.



278

279 *Fig. 3: Pressure changes in comparison with the measured data and results of Held et al. (2014). Positive pressure changes*  
 280 *represent fluid injection.*

281 A single-well circulation test in 2009 (Schindler, 2009) was used to calibrate the transmissivities of  
 282 the fractures in the southeastern part of the reservoir connected to GPK4 (Fig. 4). Strongly varying  
 283 flow rates up to the 10<sup>th</sup> day were only partially considered because their influence on the long-term  
 284 reservoir behavior is negligible. Discrepancies between simulated and measured data occurring after  
 285 110 days are probably due to disturbances in the experimental sequence. Therefore, the steady  
 286 pressure change between day 30 and 110 was used for the calibration of the hydraulic features.



287

288 *Fig. 4: Pressure changes compared with the measured data and results of Held et al. (2014) for GPK4. Missing*  
 289 *experimental data leads to zero values.*

290 The faults and fractures were calibrated for their transmissivities and the granitic matrix for the  
 291 permeability and hydraulic diffusivity (Table 2). In comparison to Held et al. (2014), the calibrated  
 292 data differs slightly. It is worthwhile noting that the fractures close to the wells affect the calibration  
 293 results decisively. Therefore, the calibrated transmissivities have a high accuracy in the vicinity of  
 294 the wells, but give only a rough estimate for the hydraulic properties of remote faults and fractures.

295 *Table 2: Calibrated transmissivities of the faults and fracture network and the permeability of the matrix.*

Name	Transmissivity [m <sup>2</sup> .s <sup>-1</sup> ]			Permeability [m <sup>2</sup> ]
GPK3-FZ4770	4.80E-05	<b>Granitic matrix</b>	<b>x</b>	1.34E-16
GPK1-FZ2856	5.00E-05		<b>y</b>	3.30E-16
GPK1-FZ2120	3.80E-04		<b>z</b>	1.65E-16
GPK3-FZ5020	1.68E-05			
GPK4-FZ4710	3.80E-05			
Soultz fault	6.80E-05			
Kutzenhausen fault	6.80E-04			
MS-GPK2-2000a	5.10E-05			
MS-GPK3-2003a	3.90E-04			
MS-GPK4-20045b	3.20E-05			
Hermerswiller fault	6.80E-05			
PS3-Int (VSP)	6.40E-04			
Separation	6.80E-05			

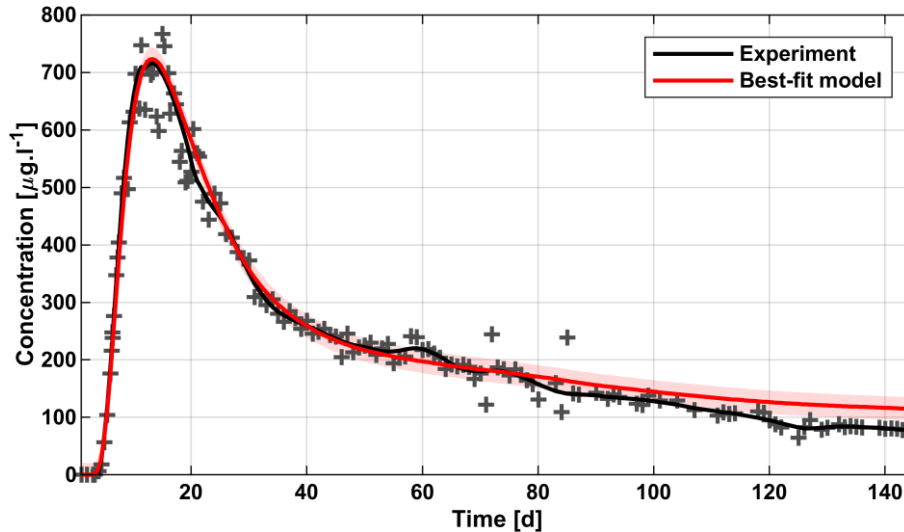
GPK3-FZ4770-GPK2  
GPK3-FZ4770-GPK3

5.65E-05  
2.95E-05

296

#### 297 4.2. Flow field

298 The findings of the circulation experiments can be coupled to multi-well tracer experiments for  
299 quantifying the inter-well connection and flow field of the Soultz geothermal reservoir. A 145-day  
300 tracer test was carried out between July and December 2005 in the wells GPK2 to GPK4 (Sanjuan  
301 et al., 2006). During the experiment, fluorescein tracer was injected in GPK3 and extracted from  
302 GPK2 and GPK4. The fluid, extracted with average flow rates of  $11.9 \text{ l.s}^{-1}$  (GPK2) and  $3.1 \text{ l.s}^{-1}$   
303 (GPK4), was reinjected in GPK3 with  $15 \text{ l.s}^{-1}$ . The fluorescein concentration during injection was  
304  $146 \text{ mg.l}^{-1}$  over 24 h. Before the first injection, 8 days of circulation provided a stationary flow field.  
305 The results of the experiment and best-fit modeling for the wells GPK2 and GPK4 are shown in Fig.  
306 5 and Fig. 7. The peak velocities of the different pathways were fitted under the assumption of the  
307 obtained transmissivities in the previous section by adapting the permeability to the expected and  
308 measured travel time and fluid velocities along the affected fractures. The mixing around the  
309 breakthrough maximum was achieved by adjusting the longitudinal and transversal dispersivity and  
310 the variation of the aperture. In addition, the 95% confidence interval as the result of the standard  
311 error of the mean modeled solute concentration is presented.

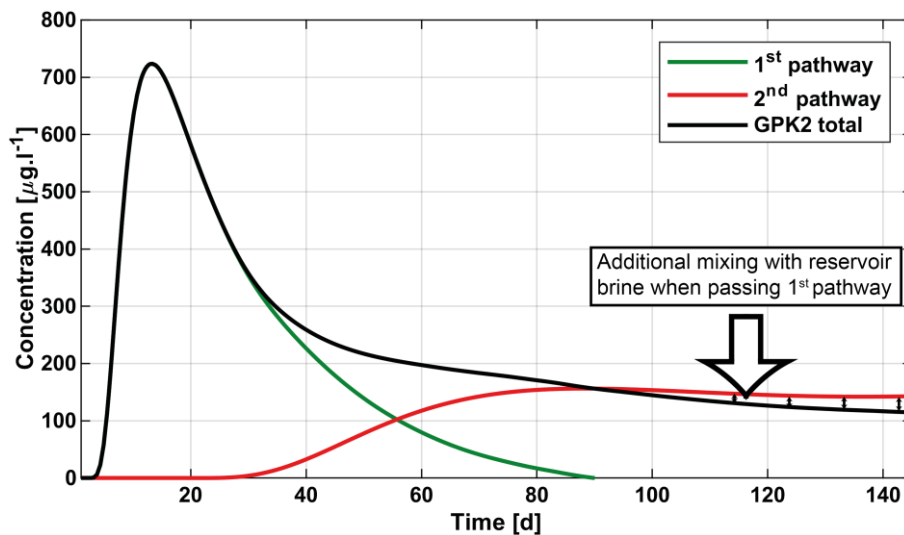


312

313 *Fig. 5: Simulated and measured fluorescein concentration at well GPK2; The grey crosses are the experimental data, and*  
314 *the black line shows their mean value. The red line shows the best-fit model with a 95% confidence interval as the red*  
315 *shadow.*

316 Fig. 5 shows the modeled and observed results of GPK2 for the tracer breakthrough curve (BTC).  
317 The maximum concentration ( $730 \text{ µg.l}^{-1}$ ), giving a peak velocity of  $2.6 \text{ m.h}^{-1}$ , was observed after  
318 13 days. A strong tailing is noticeable until the end of the experiment, which could be the result of 1)  
319 diffusive exchange with matrix, 2) dispersive effects in the fracture channeling and/or 3) the  
320 interconnection of the wells by different fracture sets (Becker and Shapiro, 2000). As shown in Fig.

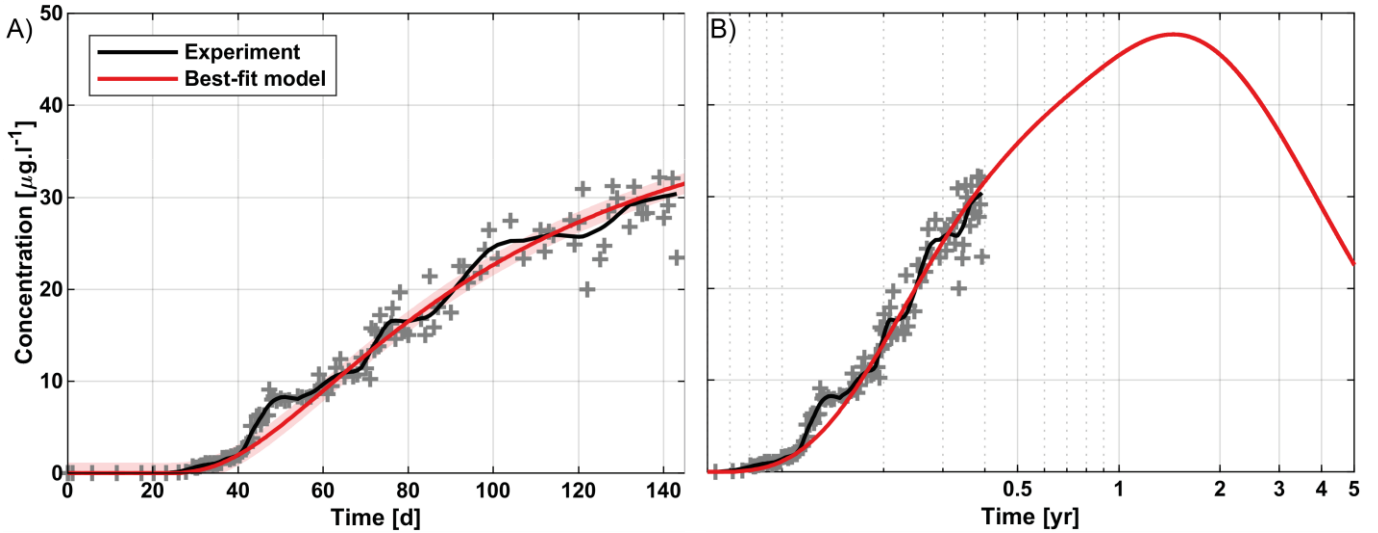
321 8 the tailing could be related to the latter option. It is possible to identify and quantify two to three  
 322 different hydraulic pathways connecting GPK3 and GPK2 (Fig. 6). The main solute influx in GPK2  
 323 was identified to occur along the fracture GPK3-FZ4770, connecting the open-hole section of GPK3  
 324 with the casing leakage of GPK2. The entire amount of tracer along this pathway was swept after  
 325 90 days of circulation. The second pathway along GPK3-FZ4770 and MS-GPK2-2000a was noticed  
 326 after 26 days and has a maximum concentration of  $161 \mu\text{g.l}^{-1}$  after 90 days with a peak velocity of  
 327  $0.5 \text{ m.h}^{-1}$ . The third pathway, along GPK3-FZ5020 and MS-GPK2-2000a, shows a strong dilution  
 328 with reservoir fluids, which is why no peak concentration can be detected in the simulation. The lower  
 329 total measured concentration compared to the second pathway tracer concentration after 90 days  
 330 (Fig. 6) can be explained by additional mixing along the well trajectory of GPK2. The mixing took  
 331 place when the higher concentrated fluid, entering the open hole section of GPK2, passed the casing  
 332 leakage on its way upwards and was mixed with the less concentrated fluid of the upper pathway.  
 333 These pathways were also confirmed in further experiments conducted in 2010 and 2013 along this  
 334 pathway (Sanjuan et al., 2015).



335  
 336 *Fig. 6: Simulated tracer concentration at the GPK2 wellhead by showing the contributions of the individual pathways*

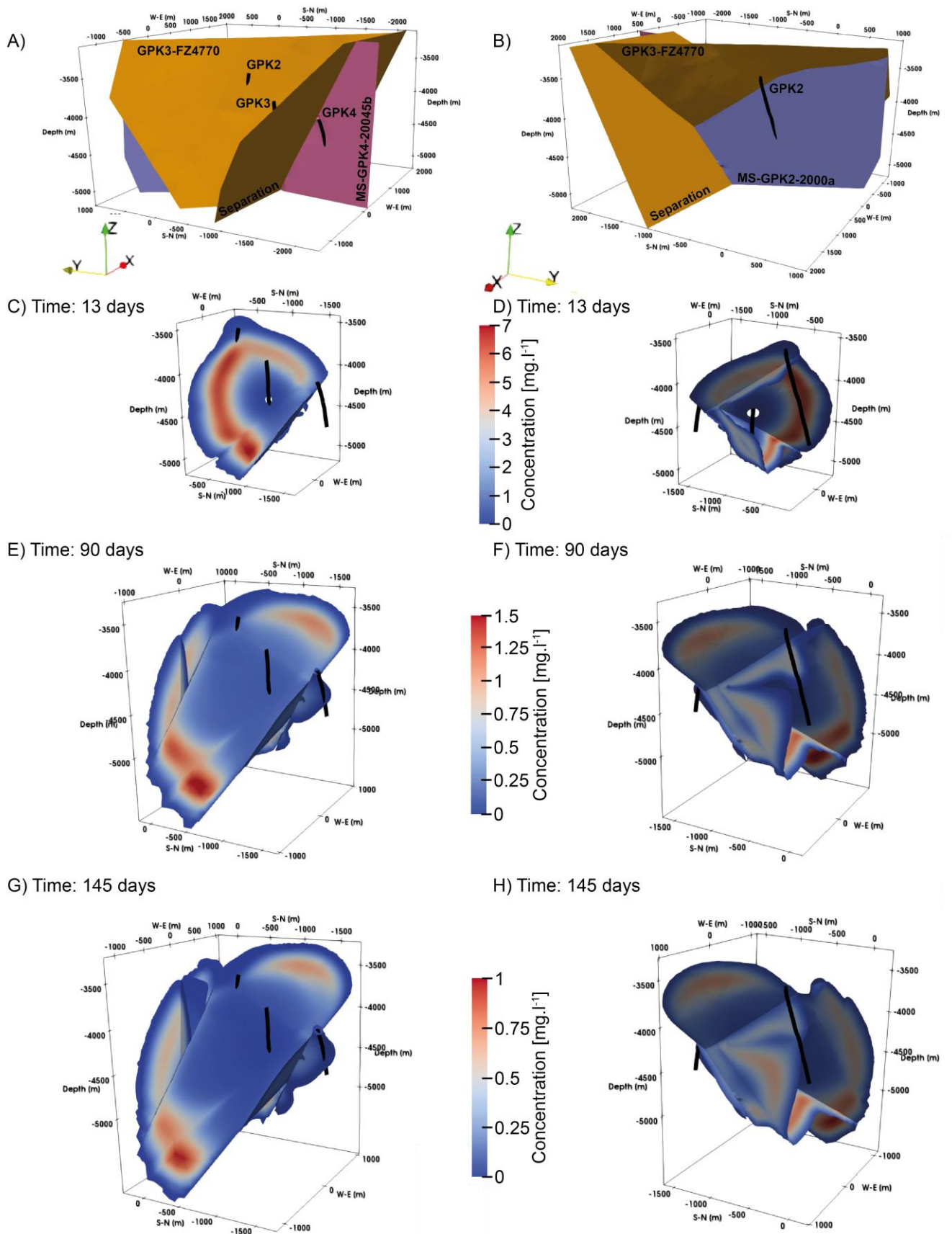
337 The result of the simulation at GPK4 in comparison to the experimental data is shown in Fig. 7. The  
 338 first arrival occurred 23 days after injection while the maximum concentration ( $31 \mu\text{g.l}^{-1}$ ) was  
 339 measured at the end of the experiment. A peak in the concentration, similar to the recorded one for  
 340 GPK2, cannot be observed within the experimental period. The BTC shows typical behavior with  
 341 clear mixing effects, such as strong dilution and no clear maximum. The reported scattered  
 342 measured data could not be reproduced in the simulation. Predictions about the mean transfer time  
 343 and maximum concentration are therefore subject to a high degree of uncertainty. Assuming a  
 344 continuous circulation and constant flow rates, the peak concentration of  $48 \mu\text{g.l}^{-1}$  was observed after  
 345 1.5 years followed by a decline to  $23 \mu\text{g.l}^{-1}$  at the end of the long-term forecast (5 years) (Fig. 7b).  
 346 The relatively late arrival time at GPK4 compared to GPK2 indicates the low fluid velocity ( $0.06 \text{ m.h}^{-1}$ )  
 347 of this pathway. Combined with the low tracer concentration and widely spread peak, a poor

348 hydraulic connection between both boreholes is clear probably due to the Separation fracture. The  
 349 fracture is oriented in WNW-ESE-direction and thus acts as an anomalous zone, which hydraulically  
 350 unlinks the two parts of the reservoir from each other by creating a preferential pathway and drainage  
 351 along itself. Fig. 8 shows the dimensionless solute concentration on the affected faults and fractures  
 352 at several time steps. The proposed different hydraulic pathways can be identified as areas with an  
 353 increased solute concentration, which allow the movement of the solute between the injection and  
 354 extraction wells.



355

356 Fig. 7: Simulated and measured dimensionless fluorescein concentration at GPK4; A) over the experimental duration; B)  
 357 long-term forecast for 5 years. The grey crosses are the experimental data, and the black line shows their mean value.  
 358 The red line is the result of the best-fit model with a 95 % confidence interval as the red shadow.



359

360

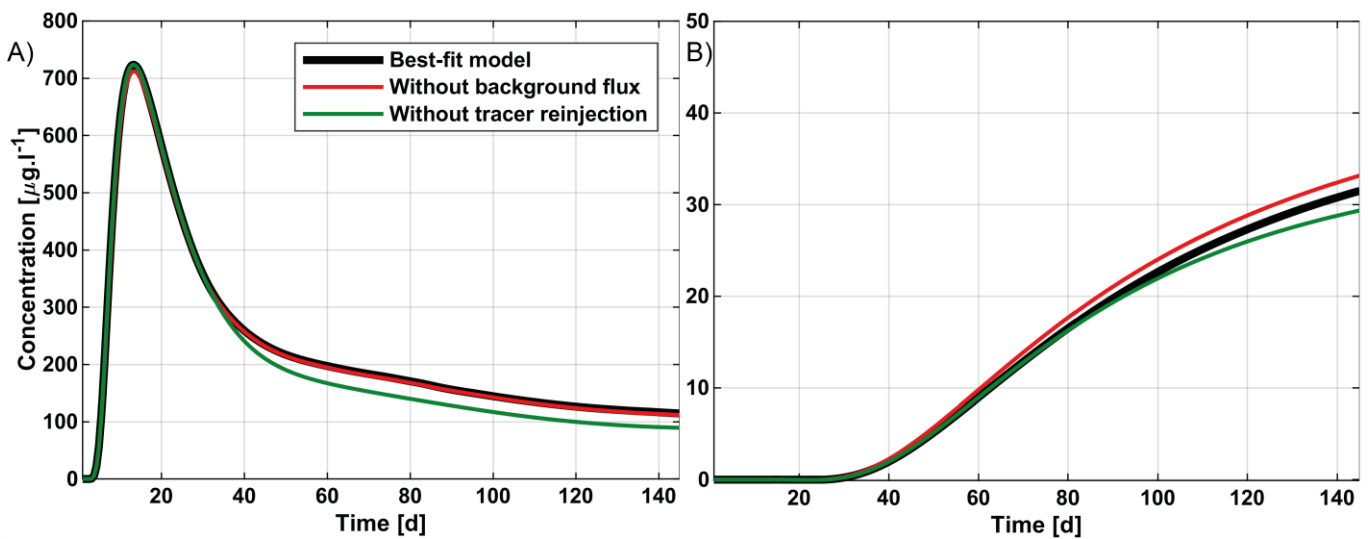
361

362

Fig. 8: Comparison of tracer concentrations in different faults and fractures. Left side) View from southwest, right side) View from the northeast. A-B) the mainly affected fractures, C-D) the tracer concentration at GPK2 reaches the maximum, E-F) the second pathway reaches the maximum and G-H) the end day of the experiment.

363 In addition to the hydraulic characterization of the DFN, effects of other factors, including tracer  
 364 reinjection and background flux, which are of great importance for the (long-term) evaluation of the  
 365 fracture network, were studied. The reinjection of the tracer-enriched produced fluid in GPK3 affected  
 366 the evolution of long-term concentrations. After the arrival of the main peak, the reinjection of  
 367 enriched fluids leads to elevated tracer concentrations along GPK3-FZ4770. At the end of the  
 368 experiment period, Fig. 9a illustrates a 20 % reduction in the tracer concentration at GPK2 if the  
 369 tracer reinjection was neglected. This factor influenced the concentration obtained for GPK4 less  
 370 prominently than for GPK2 but a 6 % reduction is still documented in Fig. 9b.

371 Another factor is the effect of the natural background flux along the main faults and fractures due to  
 372 the natural convective system of the Soultz reservoir. A minimum velocity of  $11 \text{ cm.yr}^{-1}$  reported by  
 373 Vallier et al. (2019) and fluxes for faults and fractures were accordingly calculated. However, fluid  
 374 velocity within fractures and faults generated by injection and production scenarios was dramatically  
 375 higher than the induced velocity by the background convective flux. Consequently, the influence of  
 376 this natural flux on the produced tracer concentration at GPK2 is negligible (Fig. 9a), and ignoring  
 377 this factor causes an increase of about 2% in the concentration for GPK2. For GPK4, the background  
 378 flow is opposing the available hydraulic gradient and thus lowers the recorded tracer concentrations  
 379 by around 5% at the end of the tracer experiment (Fig. 9b).



380

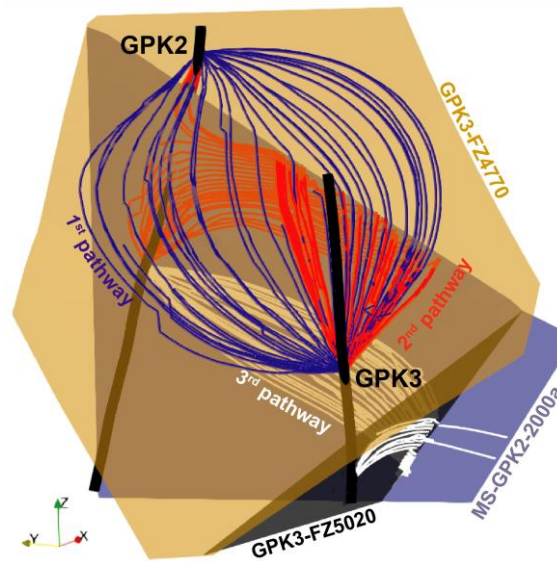
381 *Fig. 9: Sensitivity of concentration due to background flux and tracer reinjection of the wells GPK2 (A) and GPK4 (B). Note*  
 382 *the different axis scale.*

## 383 5. Discussion

384 Our results, therefore, confirm the existence of different pathways, connecting the wells of the Soultz  
 385 geothermal reservoir along different faults and fractures. The wells GPK3 and GPK2 show a good  
 386 and fast hydraulic connection, which is realized by three different pathways with different travel and  
 387 residence times. Low measurable tracer concentrations indicate a poor hydraulic connection  
 388 between GPK3 and GPK4. The convective background flux, as proposed by Sanjuan et al. (2006),



389 has a minor effect on the resulting concentrations, as the forced fluid velocities exceed the natural  
390 convective velocities by several orders of magnitude.



391

392 *Fig. 10: The main fractures and flow paths connecting the wells GPK3 and GPK2. The first pathway connects both wells*  
393 *along GPK3-FZ4770, the second pathway along GPK3-FZ4770 and MS-GPK2-2000a and the third pathway along GPK3-*  
394 *FZ5020 and MS-GPK2-2000a. The streamlines are displayed for visualizing the fracture flow.*

395 As shown in Fig. 9, re-circulated brine, containing tracers, can lead to a significant long-term increase  
396 in the overall concentration and it should be considered in momentum analysis of tracer recovery,  
397 swept volume and heat exchange area (Shook, 2005). The cumulative tracer recovery ratio,  $R_{fluor}$ ,  
398 is the sum of the recovered solutes of each pathway (Fig. 6). It can be calculated from the time-  
399 concentration plot by multiplying the concentration data with the production flow rate and the inverse  
400 of the totally injected tracer-mass. As calculated in Table 3, the total tracer recovery during the  
401 experimental period is 25.0 %, which GPK2 and GPK4 contributed 24.6 % and 0.4 %, respectively.  
402 The total recovery of the model presented is well comparable with the experimental data and the  
403 extrapolated results from it (23.5 % (Sanjuan et al., 2006) and 25.3 % (Sanjuan et al., 2015))  
404 although the individual contributions are not exactly matched. The stronger influence of the second  
405 pathway for GPK2 in the numerical simulation is partly caused by the slight overestimation after 78  
406 days as demonstrated in Fig. 6. The overestimation of the long-term values can have various causes.  
407 One possible reason are unknown fractures, which are hydraulically connected to the second  
408 pathway. Such fractures could not be considered in the model, because they were not drilled and  
409 therefore neither their geometric appearance nor their hydraulic influence on the reservoir are known  
410 (Mégel et al., 2005). Another explanation of the slight differences can be the connection of the two  
411 fractures since its internal structure is unknown, but complex flow pattern and thus mixing processes  
412 can occur here (Berkowitz et al., 1994). The neglected thermal decay of the fluorescein can also  
413 lead to slight deviations in the results, especially over a longer period of time (Adams and Davis,  
414 1991). On the other hand, considering tracer diffusion into the matrix can increase the long-term  
415 concentration results, while the peak is lowered (Ghergut et al., 2018). This simplification is

416 nevertheless permissible since there is no evidence of matrix diffusion (Radilla et al., 2012) and the  
 417 system is strongly convective, with the time scale of the transport process being significantly shorter  
 418 than that of the diffusion into the matrix (Bodin et al., 2003).

419 The swept volume can be calculated from the recovery rate. The swept volume,  $V_{swept}$ , is a measure  
 420 of the pore volume swept by tracer during an experiment as (Levenspiel 1972):

$$V_{swept} = q_{inj} * \tau * R_{fluo} \quad \text{Eq. 4}$$

421 where  $\tau$  is the mean residence time, corrected for the tracer recycling and  $q_{inj}$  is the injection rate.  
 422 Key assumptions for these calculations are a steady flow field on the affected fractures and the  
 423 usage of a conservative tracer without mass losses. The swept or pore volume for the connection of  
 424 GPK3 and GPK2 is 4000 m<sup>3</sup> for the first pathway and 10300 m<sup>3</sup> for the second pathway. The swept  
 425 volume for the first pathway and Sanjuan et al. (2006) are a perfect match, while the value of the  
 426 second pathway is rising by around 60 %, which is due to the higher recovery rate in simulations. If  
 427 a mean transfer time for GPK4 is calculated at the end of the experiment (145 days), the total swept  
 428 volume is 133 m<sup>3</sup>, which corresponds to Sanjuan et al. (2006). However, it is significantly smaller  
 429 compared to the main pathways between GPK3 and GPK2.

430 *Table 3: Summary of the recovery ratio and swept pore volume of the inter-well flow between GPK3 - GPK2 and GPK3 -*  
 431 *GPK4 as resulting from recovered solute concentrations in comparison to Sanjuan et al. (2006)*

Wells	$R_{fluo}$ [%]		$V_{swept}$ [m <sup>3</sup> ]	
	This study	Sanjuan et al. (2006)	This study	Sanjuan et al. (2006)
<b>GPK2 – 1<sup>st</sup> pathway</b>	14.5	15.6	4000	3900
<b>GPK2 – 2<sup>nd</sup> pathway</b>	10.1	7.9	10300	6500
<b>GPK4</b>	0.4	1.8	133	120
<b>Total</b>	25.0	25.3	14533	10520

432

433 The results confirm the existence of a fractured zone between the wells GPK3 and GPK4. After  
 434 calibration of the numerical model using hydraulic and tracer tests, the Separation fracture, which is  
 435 oriented WNW-ESE, could be assigned as a hydraulic conduit between the NNW-SSE striking  
 436 fractures. The fracture is connecting the northern reservoir with the main fault system and creating  
 437 a preferential fluid pathway. Since the fractures intersecting GPK4 (MS-GPK4-20045b and GPK4-  
 438 FZ4710) have a higher resistance to fluid flow than the Separation fracture, the tracer is mainly  
 439 transported and mixed along this fracture and only little amount passes to the southern reservoir and  
 440 GPK4. The results are in agreement with the microseismic inversion of Kohl et al. (2006), which  
 441 indicated a seismically inactive E-W-striking plane that could be either highly permeable or totally  
 442 sealed. Calò et al. (2016) concluded a seismic anomalous zone between the two wells from Vertical  
 443 Seismic Profiling as well. Barton et al. (1995) observed that fractures oriented perpendicular to the  
 444 maximum horizontal stress have a higher probability to be sealed. Here, the fracture possesses a

445 high hydraulic conductivity, even as the orientation is unfavorable in terms of dilation with respect to  
446 the regional stress field. Localized stress perturbations and a transition in the stress regime (from  
447 normal-faulting to strike-slip) are known for the deepest parts of the Soultz reservoir (Cuenot et al.,  
448 2006; Dorbath et al., 2010). Comparable observations could also be made for the nearby Bruchsal  
449 geothermal power plant. Several antithetic fractures have been detected, which are misaligned with  
450 the recent stress field and are a result of the complex tectonic history of the URG (Meixner et al.,  
451 2016). Those misoriented fault zones can, as indicated in this study, have an impact on the local  
452 flow field.

453 In the northern part of the reservoir, the fracture GPK3-FZ4770 creates the shortest pathway  
454 between the wells GPK3 and GPK2, with the main contribution to the inter-well flow and an average  
455 fluid velocity of  $2.6 \text{ m}\cdot\text{h}^{-1}$ . As the breakthrough curve is completely captured within the experimental  
456 time, the minimum heat exchange area for this pathway can be calculated. The minimal heat  
457 exchange surface area is the area of the fracture surfaces swept by fluid traveling from the injection  
458 to the production well assuming a parallel plate model with the known pore volume and aperture  
459 (Robinson and Tester, 1984). The area along the GPK3-FZ4770, which was analytically calculated  
460 from the pore volume swept ( $1.1 \times 10^6 \text{ m}^2$ ), is half of the area ( $2.1 \times 10^6 \text{ m}^2$ ) determined by the analysis  
461 of the streamlines between the wells in the simulation results (Fig. 10). In reality, the heat exchange  
462 area tends to be even higher due to the complex internal structure of fractures, which is simplified in  
463 the model. Fractures in the area of Soultz are typically described as zones of highly clustered shear  
464 fractures with varying aperture and length. A core zone is surrounded by a damage zone and  
465 hydrothermally altered granite (Dezayes et al., 2010). Shook (2003) developed a concept for  
466 quantifying the relationship between the flow capacity of the set of fracture channels and its storage  
467 capacity. According to this approach, the fracture GPK3-FZ4770 can be described as a set of  
468 clustered channels with non-uniform internal structure in which half of the fluid produced in the  
469 experiments passes through 27 % of the pore volume. Therefore, the heat surface area, where the  
470 exchange between the fracture and the matrix occurs, tends to be larger than calculated and  
471 simulated with the parallel plate approach. The flow field along the fracture is asymmetric. As already  
472 shown in Fig. 8, most of the fluids recovered in GPK2 originated from a relatively small area between  
473 the two boreholes. However, a great amount of the injected solute remained in deeper sections of  
474 the reservoir and the fracture GPK3-FZ4770 without ever entering the influence region of GPK2.  
475 Detailed quantification of the minimal heat exchange area for the second and third pathways, as  
476 shown in Fig. 8 is not possible as the flow and the inter-well connection occur at a set of fractures  
477 with different flow velocities and residence times, and time-concentration plot (Fig. 6) shows ongoing  
478 recovery beyond the end of the experiment. The same issues also apply to the connection between  
479 GPK3 and GPK4.

480 The new results of the deep connection of the GPK2, GPK3 and GPK4 wells allow the reassessment  
481 of the performance of the Soultz-sous-Forêts heat exchanger system. The recalibration of the  
482 hydraulic model points to rapid fluid pathways in the central-northern part of the reservoir (between  
483 GPK1 and GPK2) increasing the risk of a (thermal) breakthrough. In contrast, for the operating  
484 scheme used in the tracer experiment, short circuits are rather unlikely due to the connection to the  
485 large-scale circulation system. The same applies to the current economic operation, where reservoir  
486 brine is produced from GPK2 and reinjected into GPK3 and GPK4 wells (Mouchot et al., 2018).  
487 Moreover, it could be shown that the northernmost part of the deep reservoir (north of GPK2), as  
488 well as the connection of the separation fracture to the regional fault system, has enlarged hydraulic  
489 conductivity and thus could potentially be the target for future research and exploration. The  
490 hydraulic model presented here can be used as a basis for the design and prediction of future  
491 experiments.

## 492 **6. Conclusion**

493 In the past, many attempts have been made to describe the flow field in the Soultz geothermal  
494 reservoir. Mostly, the individual interconnections of the wells were considered separately, while a  
495 holistic and more general description of the reservoir pathways often failed. In this paper, the  
496 developed and presented concept allows the simultaneous matching of the tracer's breakthrough  
497 curves on both production wells and the qualitative and quantitative identification of the different  
498 hydraulic interconnections along the fault and fracture network based on the structural model of the  
499 Soultz reservoir.

500 The Soultz EGS can be described as a fractured reservoir connecting different wells along flow  
501 channels generated by the main hydraulic pathways. The hydraulic connection of GPK3 and GPK2  
502 was established along highly transmissive pathways with two fluorescein peak times of 13 and  
503 90 days. The main direct pathway is occurring along the fracture GPK3-FZ4770, which accounts for  
504 14.5 % of the tracer contribution. The cumulative tracer recovery of the different pathways is  
505 25 % while the total swept volume is 14533 m<sup>3</sup>. The minimal heat exchanger surface on the main  
506 pathway is 2.1x10<sup>6</sup> m<sup>2</sup>. The value is twice as large as the expected value from the analytical  
507 evaluation of the experiment. In contrast, the connection between GPK3 and GPK4 has no directly  
508 identifiable fluid pathway. The forecast modeling predicted a peak arrival after 1.5 years of  
509 continuous injection with the maximum tracer concentration which is 10 times lower than for GPK2.  
510 Only a small amount of tracer is recovered from the well GPK4 (0.4 %), and the swept pore volume  
511 is approximately two orders of magnitude smaller (133 m<sup>3</sup>) than the direct and well-established  
512 connection of GPK2. The impeded connection between GPK3 and GPK4 is presumably related to a  
513 WNW-ESE-oriented fractured zone, establishing a preferential fluid pathway, connecting the  
514 northern reservoir with the local fault network, while the southern reservoir is only connected by  
515 minor transmissive fractures to this conductive zone. According to the new hydraulic model, further

516 exploration and experimental research should focus on the connection of the Soultz geothermal  
517 reservoir to the regional fault network.

#### 518 Acknowledgments

519 We thank the anonymous reviewers for their constructive criticisms that helped to improve the quality  
520 of the manuscript. The authors acknowledge the financial support by the Federal Ministry for  
521 Economic Affairs and Energy of Germany in the project GeoFaces (No. 0324025C) and the  
522 Helmholtz portfolio project "Geoenergy". The support from the program "Renewable Energies",  
523 under the topic "Geothermal Energy Systems", is gratefully acknowledged. We also thank the EnBW  
524 Energie Baden-Württemberg AG for supporting geothermal research at KIT.

525 **References**

- 526 Adams, M.C., Davis, J., 1991. Kinetics of fluorescein decay and its application as a geothermal  
527 tracer. *Geothermics* 20 (1-2), 53–66. doi:10.1016/0375-6505(91)90005-G.
- 528 Aichholzer, C., Düringer, P., Orciani, S., Genter, A., 2016. New stratigraphic interpretation of the  
529 Soultz-sous-Forêts 30-year-old geothermal wells calibrated on the recent one from Rittershoffen  
530 (Upper Rhine Graben, France). *Geotherm Energy* 4 (1), 132. doi:10.1186/s40517-016-0055-7.
- 531 Aquilina, L., Dreuzy, J.-R. de, Bour, O., Davy, P., 2004. Porosity and fluid velocities in the upper  
532 continental crust (2 to 4 km) inferred from injection tests at the Soultz-sous-Forêts geothermal  
533 site. *Geochimica et Cosmochimica Acta* 68 (11), 2405–2415. doi:10.1016/j.gca.2003.08.023.
- 534 Aquilina, L., Rose, P., Brach, M., Gentier, S., Jeannot, R., Jacquot, E., Audigane, P., Tran-Vie, T.,  
535 Jung, R., Baumgärtner, J., Baria, R., Gérard, A., 1998. A Tracer Test at the Soultz-Sous-Forêts  
536 Hot Dry Rock Geothermal Site: PROCEEDINGS, Twenty-Third Workshop on  
537 Geothermal Reservoir Engineering, Stanford, California, 8 pp.
- 538 Ayling, B.F., Hogarth, R.A., Rose, P.E., 2016. Tracer testing at the Habanero EGS site, central  
539 Australia. *Geothermics* 63, 15–26. doi:10.1016/j.geothermics.2015.03.008.
- 540 Bächler, D., Kohl, T., Rybach, L., 2003. Impact of graben-parallel faults on hydrothermal  
541 convection—Rhine Graben case study. *Physics and Chemistry of the Earth, Parts A/B/C* 28 (9-  
542 11), 431–441. doi:10.1016/S1474-7065(03)00063-9.
- 543 Barton, C.A., Zoback, M.D., Moos, D., 1995. Fluid flow along potentially active faults in crystalline  
544 rock. *Geol* 23 (8), 683. doi:10.1130/0091-7613(1995)023<0683:FFAPAF>2.3.CO;2.
- 545 Bataillé, A., Genthon, P., Rabinowicz, M., Fritz, B., 2006. Modeling the coupling between free and  
546 forced convection in a vertical permeable slot: Implications for the heat production of an  
547 Enhanced Geothermal System. *Geothermics* 35 (5-6), 654–682.  
548 doi:10.1016/j.geothermics.2006.11.008.
- 549 Bauget, F., Fourar, M., 2007. Convective dispersion in a real fracture: PROCEEDINGS: Thirty-  
550 Second Workshop on Geothermal Reservoir Engineering Stanford University,  
551 Stanford, California, 8 pp.
- 552 Baujard, C., Bruel, D., 2006. Numerical study of the impact of fluid density on the pressure  
553 distribution and stimulated volume in the Soultz HDR reservoir. *Geothermics* 35 (5-6), 607–621.  
554 doi:10.1016/j.geothermics.2006.10.004.
- 555 Bear, J., Cheng, A.H.-D., 2010. Modeling Groundwater Flow and Contaminant Transport. Theory  
556 and Applications of Transport in Porous Media 23. Springer Science+Business Media B.V,  
557 Dordrecht. doi:10.1007/978-1-4020-6682-5.

558 Becker, M.W., Shapiro, A.M., 2000. Tracer transport in fractured crystalline rock: Evidence of  
559 nondiffusive breakthrough tailing. *Water Resour. Res.* 36 (7), 1677–1686.  
560 doi:10.1029/2000WR900080.

561 Berkowitz, B., 2002. Characterizing flow and transport in fractured geological media: A review.  
562 *Advances in Water Resources* 25 (8-12), 861–884. doi:10.1016/S0309-1708(02)00042-8.

563 Berkowitz, B., Naumann, C., Smith, L., 1994. Mass transfer at fracture intersections: An evaluation  
564 of mixing models. *Water Resour. Res.* 30 (6), 1765–1773. doi:10.1029/94WR00432.

565 Berre, I., Doster, F., Keilegavlen, E., 2018. Flow in Fractured Porous Media: A Review of Conceptual  
566 Models and Discretization Approaches. *Transp Porous Med* 137 (02), 49. doi:10.1007/s11242-  
567 018-1171-6.

568 Blumenthal, M., Kühn, M., Pape, H., Rath, V., Clauser, C., 2007. Hydraulic model of the deep  
569 reservoir quantifying the multi-well tracer test. Paper presented at EHDRA Scientific Conference,  
570 28-29 June 2007.

571 Bodin, J., Delay, F., Marsily, G. de, 2003. Solute transport in a single fracture with negligible matrix  
572 permeability: 1. fundamental mechanisms. *Hydrogeology Journal* 11 (4), 418–433.  
573 doi:10.1007/s10040-003-0268-2.

574 Brooks, A.N., Hughes, T.J.R., 1982. Streamline upwind/Petrov-Galerkin formulations for convection  
575 dominated flows with particular emphasis on the incompressible Navier-Stokes equations.  
576 *Computer Methods in Applied Mechanics and Engineering* 32 (1-3), 199–259. doi:10.1016/0045-  
577 7825(82)90071-8.

578 Bundschuh, J., Suárez Arriaga, M.C., Arriaga, M.C.S., Suárez-Arriaga, M.C., 2010. Introduction to  
579 the numerical modeling of groundwater and geothermal systems: Fundamentals of mass, energy,  
580 and solute transport in poroelastic rocks. *Multiphysics modeling 2*. CRC Press, Boca Raton Fla.  
581 u.a., XLII, 479 S.

582 Calò, M., Dorbath, C., Lubrano Lavadera, P., 2016. Can faults become barriers for deep fluid  
583 circulation? Insights from high-resolution seismic VSP tomography at the Soultz-sous-Forêts  
584 geothermal site. *Geophys. Res. Lett* 43 (17), 8986–8993. doi:10.1002/2016GL069623.

585 Cornet, F.H., Bérard, T., Bourouis, S., 2007. How close to failure is a granite rock mass at a 5km  
586 depth? *International Journal of Rock Mechanics and Mining Sciences* 44 (1), 47–66.  
587 doi:10.1016/j.ijrmms.2006.04.008.

588 Crank, J., Nicolson, P., 1996. A practical method for numerical evaluation of solutions of partial  
589 differential equations of the heat-conduction type. *Adv Comput Math* 6 (1), 207–226.  
590 doi:10.1007/BF02127704.

- 591 Cuenot, N., Charléty, J., Dorbath, L., Haessler, H., 2006. Faulting mechanisms and stress regime at  
592 the European HDR site of Soultz-sous-Forêts, France. *Geothermics* 35 (5-6), 561–575.  
593 doi:10.1016/j.geothermics.2006.11.007.
- 594 Dezayes, C., Genter, A., Valley, B., 2010. Structure of the low permeable naturally fractured  
595 geothermal reservoir at Soultz. *Comptes Rendus Geoscience* 342 (7-8), 517–530.  
596 doi:10.1016/j.crte.2009.10.002.
- 597 Dorbath, L., Evans, K., Cuenot, N., Valley, B., Charléty, J., Frogneux, M., 2010. The stress field at  
598 Soultz-sous-Forêts from focal mechanisms of induced seismic events: Cases of the wells GPK2  
599 and GPK3. *Comptes Rendus Geoscience* 342 (7-8), 600–606. doi:10.1016/j.crte.2009.12.003.
- 600 Evans, J.P., Forster, C.B., Goddard, J.V., 1997. Permeability of fault-related rocks, and implications  
601 for hydraulic structure of fault zones. *Journal of Structural Geology* 19 (11), 1393–1404.  
602 doi:10.1016/S0191-8141(97)00057-6.
- 603 Fox, D.B., Sutter, D., Beckers, K.F., Lukawski, M.Z., Koch, D.L., Anderson, B.J., Tester, J.W., 2013.  
604 Sustainable heat farming: Modeling extraction and recovery in discretely fractured geothermal  
605 reservoirs. *Geothermics* 46, 42–54. doi:10.1016/j.geothermics.2012.09.001.
- 606 Garnish, J., 2002. European activities in Hot Dry Rock research. *Open Meeting on Enhanced  
607 Geothermal Systems*, 8–9.
- 608 Gaston, D., Newman, C., Hansen, G., Lebrun-Grandié, D., 2009. MOOSE: A parallel computational  
609 framework for coupled systems of nonlinear equations. *Nuclear Engineering and Design* 239  
610 (10), 1768–1778. doi:10.1016/j.nucengdes.2009.05.021.
- 611 Genter, A., Baujard, C., Cuenot, N., Dezayes, C., Kohl, T., Masson, F., Sanjuan, B., Scheiber, J.,  
612 Schill, E., Schmittbuhl, J., Vidal, J., 2016. Geology, Geophysics and Geochemistry in the Upper  
613 Rhine Graben: the frame for geothermal energy use. *European Geothermal Congress 2016*,  
614 5 pp.
- 615 Genter, A., Cuenot, N., Goerke, X., Moeckes, W., Scheiber, J., 2011. Scientific and technical activity  
616 of the Soultz geothermal power plant, Progress report from December 2010 to June 2011: GEIE  
617 report RA05 002, 59 pp.
- 618 Genter, A., Evans, K., Cuenot, N., Fritsch, D., Sanjuan, B., 2010. Contribution of the exploration of  
619 deep crystalline fractured reservoir of Soultz to the knowledge of enhanced geothermal systems  
620 (EGS). *Comptes Rendus Geoscience* 342 (7-8), 502–516. doi:10.1016/j.crte.2010.01.006.
- 621 Gentier, S., Rachez, X., Ngoc, T.D.T., Peter-Borie, M., Souque Christine, 2010. 3D Flow Modelling  
622 of the Medium-Term Circulation Test Performed in the Deep Geothermal Site of Soultz-Sous-  
623 forêts (France): PROCEEDINGS World Geothermal Congress 2010, Bali, Indonesia, 13 pp.



- 624 Gentier, S., Rachez, X., Peter-Borie, M., Blaisonneau, A., Sanjuan, B., 2011. Transport and Flow  
625 Modelling of the Deep Geothermal Exchanger Between Wells at Soultz-sous-Forêts (France).  
626 GRC Transactions 35, 363–369.
- 627 Gérard, A., Genter, A., Kohl, T., Lutz, P., Rose, P., Rummel, F., 2006. The deep EGS (Enhanced  
628 Geothermal System) project at Soultz-sous-Forêts (Alsace, France). *Geothermics* 35 (5-6), 473–  
629 483. doi:10.1016/j.geothermics.2006.12.001.
- 630 Gessner, K., Kühn, M., Rath, V., Kosack, C., Blumenthal, M., Clauser, C., 2009. Coupled Process  
631 Models as a Tool for Analysing Hydrothermal Systems. *Surv Geophys* 30 (3), 133–162.  
632 doi:10.1007/s10712-009-9067-1.
- 633 Ghergut, I., Behrens, H., Sauter, M., Licha, T., Nottebohm, M., 2013. Can Peclet numbers depend  
634 on tracer species? going beyond SW test insensitivity to advective or equilibrium-exchange  
635 processes.: PROCEEDINGS, Thirty-Eighth Workshop on Geothermal Reservoir Engineering,  
636 Stanford, California, 10 pp.
- 637 Ghergut, J., Behrens, H., Bansabat, J., Sauter, M., Wagner, B., Wiegand, B., 2018. Sorption, matrix  
638 diffusion, ... need not make a major difference for frac characterization from short-term tracer  
639 signals: PROCEEDINGS, 43<sup>rd</sup> Workshop on Geothermal Reservoir Engineering,  
640 Stanford, California, 13 pp.
- 641 Ghergut, J., Behrens, H., Sauter, M., 2016. Petrothermal and aquifer-based EGS in the Northern-  
642 German Sedimentary Basin, investigated by conservative tracers during single-well injection-  
643 flowback and production tests. *Geothermics* 63, 225–241.  
644 doi:10.1016/j.geothermics.2016.01.015.
- 645 Gholami Korzani, M., Held, S., Kohl, T., 2019. Numerical based filtering concept for feasibility  
646 evaluation and reservoir performance enhancement of hydrothermal doublet systems.  
647 Submitted. *Journal of Petroleum Science and Engineering*.
- 648 Guillou-Frottier, L., Carré, C., Bourguine, B., Bouchot, V., Genter, A., 2013. Structure of hydrothermal  
649 convection in the Upper Rhine Graben as inferred from corrected temperature data and basin-  
650 scale numerical models. *Journal of Volcanology and Geothermal Research* 256, 29–49.  
651 doi:10.1016/j.jvolgeores.2013.02.008.
- 652 Hadermann, J., Heer, W., 1996. The Grimsel (Switzerland) migration experiment: integrating field  
653 experiments, laboratory investigations and modelling. *Journal of Contaminant Hydrology* 21 (1-  
654 4), 87–100. doi:10.1016/0169-7722(95)00035-6.

- 655 Held, S., Genter, A., Kohl, T., Kölbl, T., Sausse, J., Schoenball, M., 2014. Economic evaluation of  
656 geothermal reservoir performance through modeling the complexity of the operating EGS in  
657 Soultz-sous-Forêts. *Geothermics* 51, 270–280. doi:10.1016/j.geothermics.2014.01.016.
- 658 Hettkamp, T., Fuhrmann, G., Rummel, F., 1999. Hydraulic properties of the Rheingraben basement  
659 material. *Bulletin d'Hydrogéologie* No 17.
- 660 Hooijkaas, G.R., Genter, A., Dezayes, C., 2006. Deep-seated geology of the granite intrusions at  
661 the Soultz EGS site based on data from 5km-deep boreholes. *Geothermics* 35 (5-6), 484–506.  
662 doi:10.1016/j.geothermics.2006.03.003.
- 663 Iglesias, E.R., Flores-Armenta, M., Torres, R.J., Ramirez-Montez, M., Reyes-Picaso, N., Cruz-  
664 Grajales, I., 2015. Tracer Testing at Los Humeros, Mexico, High-Enthalpy Geothermal Field:  
665 PROCEEDINGS World Geothermal Congress 2015, Melbourne, 8 pp.
- 666 Jung, R., Schindler, M., Nami, P., Tischner, T., 2010. Determination of flow exits in the Soultz  
667 borehole GPK2 by using the brine displacement method. *Comptes Rendus Geoscience* 342 (7-  
668 8), 636–643. doi:10.1016/j.crte.2009.06.002.
- 669 Karmakar, S., Ghergut, J., Sauter, M., 2016. Early-flowback tracer signals for fracture  
670 characterization in an EGS developed in deep crystalline and sedimentary formations: a  
671 parametric study. *Geothermics* 63, 242–252. doi:10.1016/j.geothermics.2015.08.007.
- 672 Kestin, J., Khalifa, H.E., Correia, R.J., 1981. Tables of the dynamic and kinematic viscosity of  
673 aqueous KCl solutions in the temperature range 25–150 °C and the pressure range 0.1–35 MPa.  
674 *Journal of Physical and Chemical Reference Data* 10 (1), 57–70. doi:10.1063/1.555640.
- 675 Kohl, T., Bächler, D., Rybach, L., 2000. Steps towards a comprehensive thermo-hydraulic analysis  
676 of the HDR test site Soultz-sous-Forêts. *Proc. World Geothermal Congress*, 3459–3464.
- 677 Kohl, T., Baujard, C., Mégel, T., 2006. Conditions for mechanical re-stimulation of GPK4. Paper  
678 presented at EHDRA Scientific Conference, 15-16 June 2006.
- 679 Kohl, T., Mégel, T., 2007. Predictive modeling of reservoir response to hydraulic stimulations at the  
680 European EGS site Soultz-sous-Forêts. *International Journal of Rock Mechanics and Mining*  
681 *Sciences* 44 (8), 1118–1131. doi:10.1016/j.ijrmms.2007.07.022.
- 682 Kosack, C., Vogt, C., Rath, V., Marquart, G., 2011. Stochastic Estimates of the Permeability Field of  
683 the Soultz-sous-Forêts Geothermal Reservoir - Comparison of Bayesian Inversion, MC  
684 Geostatistics, and EnKF Assimilation: PROCEEDINGS, Thirty-Sixth Workshop on Geothermal  
685 Reservoir Engineering, Stanford.

- 686 Mégel, T., Kohl, T., Gérard, A., Rybach, L., Hopkirk, R., 2005. Downhole Pressures Derived from  
687 Wellhead Measurements during Hydraulic Experiments: PROCEEDINGS World  
688 Geothermal Congress 2005, Antalya, Turkey, 6 pp.
- 689 Meixner, J., Schill, E., Grimmer, J.C., Gaucher, E., Kohl, T., Klingler, P., 2016. Structural control of  
690 geothermal reservoirs in extensional tectonic settings: An example from the Upper Rhine Graben.  
691 *Journal of Structural Geology* 82, 1–15. doi:10.1016/j.jsg.2015.11.003.
- 692 Moreno, L., Tsang, Y.W., Tsang, C.F., Hale, F.V., Neretnieks, I., 1988. Flow and tracer transport in  
693 a single fracture: A stochastic model and its relation to some field observations. *Water Resour.*  
694 *Res.* 24 (12), 2033–2048. doi:10.1029/WR024i012p02033.
- 695 Mouchot, J., Genter, A., Cuenot, N., Scheiber, J., Seibel, O., Bosia, C., Ravier, G., 2018. First Year  
696 of Operation from EGS geothermal Plants in Alsace, France: Scaling Issues: PROCEEDINGS,  
697 43<sup>rd</sup> Workshop on Geothermal Reservoir Engineering, 12 pp.
- 698 O’Sullivan, M.J., Pruess, K., Lippmann, M.J., 2001. State of the art of geothermal reservoir  
699 simulation. *Geothermics* 30 (4), 395–429. doi:10.1016/S0375-6505(01)00005-0.
- 700 Pfender, M., Nami, P., Tischner, T., Jung, R., 2006. Status of the Soultz deep wells based on low  
701 rate hydraulic tests and temperature logs. EHDRA Scientific Conference 15.-16.06.
- 702 Place, J., Sausse, J., Marthelot, J.-M., Diraison, M., Géraud, Y., Naville, C., 2011. 3-D mapping of  
703 permeable structures affecting a deep granite basement using isotropic 3C VSP data.  
704 *Geophysical Journal International* 186 (1), 245–263. doi:10.1111/j.1365-246X.2011.05012.x.
- 705 Pribnow, D., Schellschmidt, R., 2000. Thermal tracking of upper crustal fluid flow in the Rhine  
706 graben. *Geophys. Res. Lett* 27 (13), 1957–1960. doi:10.1029/2000GL008494.
- 707 Radilla, G., Sausse, J., Sanjuan, B., Fourar, M., 2012. Interpreting tracer tests in the enhanced  
708 geothermal system (EGS) of Soultz-sous-Forêts using the equivalent stratified medium  
709 approach. *Geothermics* 44, 43–51. doi:10.1016/j.geothermics.2012.07.001.
- 710 Robinson, B.A., Tester, J.W., 1984. Dispersed fluid flow in fractured reservoirs: An analysis of tracer-  
711 determined residence time distributions. *J. Geophys. Res. Solid Earth* 89 (B12), 10374–10384.  
712 doi:10.1029/JB089iB12p10374.
- 713 Rose, P., Leecaster, K., Drakos, P., Robertson-Tait, A., 2009. Tracer Testing at the Desert Peak  
714 EGS Project. *GRC Transactions* 33, 241–249.
- 715 Sanjuan, B., Brach, M., Genter, A., Sanjuan, R., Scheiber, J., Touzelet, S., 2015. Tracer testing of  
716 the EGS site at Soultz-sous-Forêts (Alsace, France) between 2005 and 2013: Proceedings World  
717 Geothermal Congress 2015, Melbourne, 12 pp.

- 718 Sanjuan, B., Pinault, J.-L., Rose, P., Gérard, A., Brach, M., Braibant, G., Crouzet, C., Foucher, J.-  
719 C., Gautier, A., Touzelet, S., 2006. Tracer testing of the geothermal heat exchanger at Soultz-  
720 sous-Forêts (France) between 2000 and 2005. *Geothermics* 35 (5-6), 622–653.  
721 doi:10.1016/j.geothermics.2006.09.007.
- 722 Sausse, J., Dezayes, C., Dorbath, L., Genter, A., Place, J., 2010. 3D model of fracture zones at  
723 Soultz-sous-Forêts based on geological data, image logs, induced microseismicity and vertical  
724 seismic profiles. *Comptes Rendus Geoscience* 342 (7-8), 531–545.  
725 doi:10.1016/j.crte.2010.01.011.
- 726 Sausse, J., Genter, A., 2005. Types of permeable fractures in granite. Geological Society, London,  
727 Special Publications 240 (1), 1–14. doi:10.1144/GSL.SP.2005.240.01.01.
- 728 Schill, E., Genter, A., Cuenot, N., Kohl, T., 2017. Hydraulic performance history at the Soultz EGS  
729 reservoirs from stimulation and long-term circulation tests. *Geothermics* 70, 110–124.  
730 doi:10.1016/j.geothermics.2017.06.003.
- 731 Schindler, M., 2009. Hydraulic Data recorded during the three circulations with down-hole pumps at  
732 soultz, Rapport Public GEIE n° RAP 71 000 V00. GEIE, Soultz-sous-Forêts, France,, 20 pp.
- 733 Schindler, M., Baumgärtner, J., Gandy, T., Hauffe, P., Hettkamp, T., Menzel, H., Penzkofer, P., Teza,  
734 D., Tischner, T., Wahl, G., 2010. Successful Hydraulic Stimulation Techniques for Electric Power  
735 Production in the Upper Rhine Graben, Central Europe: PROCEEDINGS World Geothermal  
736 Congress 2010, Bali, Indonesia, 7 pp.
- 737 Schmittbuhl, J., Steyer, A., Jouniaux, L., Toussaint, R., 2008. Fracture morphology and viscous  
738 transport. *International Journal of Rock Mechanics and Mining Sciences* 45 (3), 422–430.  
739 doi:10.1016/j.ijrmms.2007.07.007.
- 740 Shook, G.M., 2003. A simple, fast method of estimating fractured reservoir geometry from tracer  
741 tests. *GRC Transactions* (27), 407–411.
- 742 Shook, G.M., 2005. A systematic method for tracer test analysis: An example using Beoware tracer  
743 data: PROCEEDINGS, Thirtieth Workshop on Geothermal Reservoir Engineering,  
744 Stanford, California, 6 pp.
- 745 Stober, I., Bucher, K., 2007. Hydraulic properties of the crystalline basement. *Hydrogeol J* 15 (2),  
746 213–224. doi:10.1007/s10040-006-0094-4.
- 747 Tsang, Y.W., Tsang, C.F., Neretnieks, I., Moreno, L., 1988. Flow and tracer transport in fractured  
748 media: A variable aperture channel model and its properties. *Water Resour. Res.* 24 (12), 2049–  
749 2060. doi:10.1029/WR024i012p02049.

- 750 Vallier, B., Magnenet, V., Schmittbuhl, J., Fond, C., 2019. Large scale hydro-thermal circulation in  
751 the deep geothermal reservoir of Soultz-sous-Forêts (France). *Geothermics* 78, 154–169.  
752 doi:10.1016/j.geothermics.2018.12.002.
- 753 Vidal, J., Genter, A., 2018. Overview of naturally permeable fractured reservoirs in the central and  
754 southern Upper Rhine Graben: Insights from geothermal wells. *Geothermics* 74, 57–73.  
755 doi:10.1016/j.geothermics.2018.02.003.
- 756 Vogt, C., Marquart, G., Kosack, C., Wolf, A., Clauser, C., 2012. Estimating the permeability  
757 distribution and its uncertainty at the EGS demonstration reservoir Soultz-sous-Forêts using the  
758 ensemble Kalman filter. *Water Resour. Res.* 48 (8), 393. doi:10.1029/2011WR011673.
- 759 Zang, A., Oye, V., Jousset, P., Deichmann, N., Gritto, R., McGarr, A., Majer, E., Bruhn, D., 2014.  
760 Analysis of induced seismicity in geothermal reservoirs – An overview. *Geothermics* 52, 6–21.  
761 doi:10.1016/j.geothermics.2014.06.005.
- 762 Ziegler, P.A., Dèzes, P., 2005. Evolution of the lithosphere in the area of the Rhine Rift System. *Int*  
763 *J Earth Sci (Geol Rundsch)* 94 (4), 594–614. doi:10.1007/s00531-005-0474-3.